HHS Public Access

Author manuscript

*J Pathol*. Author manuscript; available in PMC 2023 February 11.

Published in final edited form as:

*J Pathol*. 2020 August ; 251(4): 400–410. doi:10.1002/path.5474.

# Three-dimensional analysis of extrahepatic cholangiocarcinoma and tumor budding

**Tadashi Yoshizawa**[1,2], **Seung-Mo Hong**[3], **DongJun Jung**[4], **Michaël Noë**[5], **Ashley Kiemen**[6], **Pei-Hsun Wu**[6], **Denis Wirtz**[1,6], **Ralph H Hruban**[1,5], **Laura D Wood**[1,5], **Kiyoko Oshima**[1,*]

[1]Department of Pathology, Johns Hopkins Medical Institutions, Baltimore, MD, USA

[2]Department of Pathology and Bioscience, Hirosaki University Graduate School of Medicine, Hirosaki, Japan

[3]Department of Pathology, Asan Medical Center, University of Ulsan College of Medicine, Seoul, Republic of Korea

[4]Department of Medicine, Graduate school, University of Ulsan, Seoul, Republic of Korea

[5]Department of Oncology, The Sol Goldman Pancreatic Cancer Research Center, Johns Hopkins Medical Institutions, Baltimore, MD, USA

[6]Department of Chemical and Biomolecular Engineering, Johns Hopkins University, Baltimore, MD, USA

## Abstract

Advances in tissue clearing and microscopy make it possible to study human diseases in three dimensions (3D). High-grade tumor budding is known to be associated with poor prognosis in various cancers; however, little is known about the 3D architecture of tumor budding. Using tissue clearing, we analyzed the 3D structure of tumor budding and E-cadherin expression in 31 extrahepatic cholangiocarcinomas. A total of 31 thick slabs (up to 5 mm) were harvested from surgically resected tumor tissue, including 27 hilar and 4 distal cholangiocarcinomas. Twenty-eight cases were adenocarcinoma, and three were undifferentiated carcinoma. After clearing, the tissues were immunolabeled with antibodies to cytokeratin 19 and to E-cadherin, and then visualized using light-sheet and confocal laser scanning microscopy. Tumor budding was evaluated in hematoxylin and eosin–stained sections (2D) using standard pathological criteria. Of the 31 cancers, 13 showed low-grade tumor budding and 18 showed high-grade tumor budding. First, 3D analysis revealed that the neoplastic cells in tumor buds of adenocarcinoma were typically not individual islands of cells, but rather tips of attenuated protrusions connected to the main tumor. Second, adenocarcinomas with low-grade tumor budding were composed predominantly of tubules that only focally form cords at the periphery. By

*Correspondence to: K Oshima, Department of Pathology, Johns Hopkins Medical Institutions, Weinberg Building Room 2333, 401 N. Broadway, Baltimore, MD 21231, USA. koshima3@jhmi.edu.

Author contributions statement

TY, SH, MN, RH, LW, and KO designed the research. TY, SH, and DJ carried out experimental work. TY and DJ performed computational work. TY, AK, PW, and DW analyzed interpretation data. TY and KO wrote the original manuscript, and KO, LW, and RH edited the manuscript. All authors read and approved the final manuscript.

LDW is an Associate Editor of The Journal of Pathology. No other conflicts of interest were declared.

contrast, adenocarcinomas with high-grade tumor budding predominantly formed cords in both centers and peripheries of the tumors. Third, adenocarcinoma with low-grade tumor budding was characterized by a few short protrusions with few branches, whereas adenocarcinoma with high-grade tumor budding was characterized by longer protrusions with more branching. Finally, immunolabeling of E-cadherin was stronger in the center of the adenocarcinoma but decreased at the tips of protrusions. E-cadherin loss was more extensive in the protrusions of high-grade tumor budding than in the protrusions of low-grade tumor budding. Our findings suggest that tumor buds as seen in 2D are, in fact, cross-sections of attenuated but contiguous protrusions extending from the main tumor.

### Keywords

bile ducts; neoplasia; 3D imaging; confocal microscopy

## Introduction

The prognosis for patients with cholangiocarcinoma is dismal because usually the disease is advanced at the time of diagnosis, rendering surgical removal and a cure difficult, if not impossible. Even when surgery is possible, there are often local or distant recurrences after surgery. Therefore, elucidation of the mechanism of tumor invasion leading to metastasis at the invasive front is important to predict prognosis as well as to understand the mechanisms that eventually lead to metastasis.

Tumor budding (TB), which is defined as the presence of single cells or small clusters of four neoplastic cells or less, on standard hematoxylin and eosin (H&E)–stained sections was first identified in colorectal cancer. High-grade TB has been established as a poor prognostic indicator that may be helpful for patient stratification [1,2]. TB has also been recognized as prognostic factor in other types of cancer, including gastric adenocarcinoma [3–7], esophageal squamous cell carcinoma [8–10], pancreatic adenocarcinoma [11–13], ampullary adenocarcinoma [14],head and neck squamous cell carcinoma [15–19], breast cancer [20], and bladder cancer [21]. In addition, TB has been reported to be a useful prognostic factor for cholangiocarcinoma [22–24]. Although the biological mechanism of TB and poor patient prognosis is not clear, it has been hypothesized that TB is related to the epithelial-mesenchymal transition (EMT), based on its morphological and molecular characteristics [25,26].

In two-dimensional (2D) H&E-stained sections, tumor buds appear to be isolated single neoplastic cells or small clusters of neoplastic cells detached from the main tumor. The neoplastic cells in tumor buds have been reported to show a loss of epithelial markers such as E-cadherin and an increase in mesenchymal markers such as vimentin [22]. However, little is known about the three-dimensional (3D) architecture of tumor buds. Bronsert *et al* studied the 3D architecture of tumor buds in human adenocarcinomas by reconstructing serial immunohistochemical slides, and they observed that tumor buds with detached appearance in 2D represent cell clusters that were protruding from, but still connected to, the main tumor [27]. The same study also reported decreased E-cadherin

expression and increased zinc finger E-box binding homeobox 1 (ZEB1) expression in tumor buds. However, this study was a relatively small cohort of multiple tumors, and the 3D architecture of cholangiocarcinoma was not fully defined. Tanaka *et al* examined cleared solid human tumors by light-sheet fluorescence microscopy and observed heterogeneity in immunolabeling for EMT markers in three dimensions [28]. However, quantitative 3D analysis of EMT markers has not been performed.

Recently, advances in tissue clearing, antibody penetration, and microscopy offer the potential to obtain detailed 3D images of cancer tissue. We have previously demonstrated the utility of this new technique in obtaining 3D images of invasive pancreatic cancers [29,30]. Here, using clearing, we analyzed the 3D architecture of extrahepatic cholangiocarcinoma and TB, and we couple this with an analysis of the patterns of E-cadherin expression, a marker of EMT.

## Materials and methods

### Patients and tissue preparation

We investigated 31 slabs (up to 20 × 10 × 5 mm) of extrahepatic cholangiocarcinoma from patients who underwent surgical resection at the Johns Hopkins Hospital or at the Asan Medical Center. Approval of the relevant institutional review boards was obtained. Twenty-nine samples were obtained at Johns Hopkins Hospital, and two were from the Asan Medical Center. Patients who received neoadjuvant chemotherapy or neoadjuvant radiation therapy were excluded.

### Fresh samples

Ten fresh cholangiocarcinoma tissues were processed as described previously [29,30]. In brief, the fresh tissues were fixed in 80% methanol and 20% dimethyl sulfoxide (DMSO). On the following day, tissues were fixed in 4% paraformaldehyde for 24 h at 4 °C. Next, these tissues were dehydrated with a series of methanol washes (50%, 80%, and 90%, and 3 × 100% methanol). Following this, the samples were cooled for 60 min at 4 °C and then incubated overnight in 66% dichloromethane/33% methanol at room temperature. The tissue samples then were washed two times with 100% methanol, after which 5% hydrogen peroxide was added and incubated overnight at 4 °C to oxidize endogenous pigments and auto-fluorescent proteins. The tissues were rehydrated with a series of washes (90%, 80%, and 50% methanol, and 1 × PBS) and then washed twice for an hour each in 1 × PBS/0.2%Triton X-100 (Millipore Sigma, St. Louis, MO, USA). Finally, these tissues were incubated for 2 days in a permeabilization solution of 1 × PBS/20% DMSO/0.2%Triton X-100/0.3 M glycine at 37 °C. The samples were then incubated for 2 days in a blocking reagent comprised of 1 × PBS/0.2%Triton X-100/10%DMSO/6% donkey serum.

### Formalin-fixed, paraffin-embedded (FFPE) samples

As described previously, the 21 FFPE tissues were released from the paraffin wax by incubating twice in xylene at 37 °C for 3 h each [29,30]. The tissues were washed three times in 100% methanol after which they were incubated overnight in 66% dichloromethane/33% methanol at room temperature. Following this, 5% hydrogen peroxide

was added, and the tissues were incubated overnight at 4 °C. The tissues were then rehydrated using a series of washes (90%, 80%, and 50% methanol, and 1 × PBS) and then washed twice for 60 min each in 1 × PBS/0.2%Triton X-100 and incubated for 2 days in a permeabilization solution of 1 × PBS/20% DMSO/0.2% Triton X-100/0.3 M glycine at 37 °C. The samples were then incubated for 2 days in a blocking reagent comprising 1 × PBS /0.2%Triton X-100/10%DMSO/6%.

## Immunolabeling

Two primary antibodies, cytokeratin 19 (CK19; EP1580Y, rabbit monoclonal; final concentration, 1:200; Abcam, Cambridge, UK) and E-cadherin (M168, mouse monoclonal; final concentration, 1:150; Abcam) were used for immunolabeling. To allow antibody penetration, the antibody concentration was gradually increased over 5 days. In addition, centrifugal flow was used to promote antibody penetration. During 5 days of antibody incubation, the tissues were alternatively centrifuged for 12 h at 600 × *g* and then shaken for 12 h at 37 °C. After the primary antibody was applied to the tissues, the tissues were washed five times with 1 x PBS/0.2% Tween-20 with 10 mg/ml heparin for 60 min each at room temperature. The sections were the incubated in Alexa Fluor 488-conjugated AffiniPure F (ab')$_2$ fragment donkey anti-rabbit IgG (Jackson ImmunoResearch, West Grove, PA, USA), and a Cyanine 3-conjugated AffiniPure F(ab')$_2$ fragment, donkey anti-mouse IgG (Jackson ImmunoResearch), for 4 days and protected from light. In selected cases, cell nuclei were visualized by adding 4'6-diamino-2-phenylindole (DAPI; concentration 1:500, Sigma-Aldrich) at the same time as the secondary antibody. During this procedure, the tissues were also alternatively centrifuged for 12 h at 600 × *g* and shaken for 12 h at 37 °C. The tissues were then washed five times with 1 × PBS/0.2% Tween-20 with 10 mg/ml heparin for 60 min each at room temperature.

## Tissue clearing

As described previously, the tissues were dehydrated using a series of methanol washes (50%, 80%, and 90%, and 3 × 100% methanol) each for 60 min, after which they were incubated with 66% dichloromethane/33% methanol for 3 h, and twice with 100% dichloromethane for 15 min. Finally, the tissues were transferred to dibenzyl ether (DBE) overnight at 4 °C [29,30].

## Sample imaging

Cleared immunolabeled tissues were imaged primarily with a Light Sheet Microscope (Ultramicroscope II; LaVision BioTec, Bielefeld, Germany) equipped with a Neo sCMOS camera (Andor Technology, Belfast, UK) and a 4 × objective lens immersed in DBE in the imaging chamber. To obtain high magnification images, a confocal laser scanning microscope (LSM800; Carl Zeiss, Jena, Germany) with ×5, ×10, and ×20 objectives was used.

The Alexa 488 signals from epithelial cells (normal bile duct cells and neoplastic cells) were visualized using a bandpass filter set with an excitation range of 421/50 nm and an emission range of 480/40 nm. To detect the E-cadherin antibody labeling, the Cy3 signals were visualized using a filter set with an excitation range of 550/40 nm and an emission range

of 570/50 nm. DAPI labeling of nuclei was visualized with a filter set with an excitation range of 400/40 nm and an emission range of 421/50 nm. 3D and surface-rendering image construction were performed using IMARIS software (Ver. 9.4, Bitplane, Zurich, Switzerland).

### Validation of observations made in cleared tissues

When fresh tissue was available, sections next to the fresh tissue harvested for clearing were processed for the FFPE blocks. These were sectioned at 4 μm thickness and stained with H&E for microscopic examination. When fresh tissue was unavailable, FFPE sample tissues were cleared. After the area of TB was marked on H&E slides, the same lesion in fresh tissue or FFPE tissue was evaluated on 3D images.

Grading of adenocarcinoma was assessed based on the proportion of gland formation in the tumor according to the 8th edition of the AJCC classification system [31]. Well-differentiated carcinomas were defined as having greater than 95% of the tumor composed of glands, moderately differentiated as having 50–95% of the tumor composed of glands, poorly differentiated as having less than 50% of the tumor composed of glands, and undifferentiated carcinoma as having no gland formation or mucin, and no squamous or neuroendocrine differentiation. TB was defined on H&E (2D) sections as single cells or clusters composed of fewer than five cells, and budding was classified into low (0–4 buds) and high (≥5) budding cases counted in the highest density of tumor buds at the invasive front (per ×200 magnification field, 0.785 $mm^2$) [22]. Two pathologists (TY and KO) graded the differentiation of the carcinoma and evaluated the TB status. When two pathologists did not agree, discrepancy was resolved with discussion.

### Pathological evaluation and statistical analysis

Using filament tracer analysis of IMARIS software, the morphological differences of protrusions between low-grade and high-grade TB cases in 3D were analyzed. We compared the number of branching points and the median value of protrusion length per a fixed volume (500 μm × 500 μm × 100 μm).

In addition, using volume calculating analysis of IMARIS software, we analyzed and compared the volume ratio of E-cadherin/CK19 expression in high-grade and low-grade TB cases per a fixed volume (500 μm × 500 μm × 100 μm). Imaging thresholding using the display adjustment functions of IMARIS software was utilized to remove the autofluorescence and artifacts before the analysis.

Statistical comparisons of the morphological and the volume ratio differences between low-grade and high-grade TB were analyzed by the Mann–Whitney test using R statistical programming language (http://r-project.org). Results were deemed statistically significant if $p < 0.05$.

# Results

## Patients and 2D analysis

The median age of the patients was 65 years (range 43–78 years). There were 27 patients with hilar cholangiocarcinoma and 4 with distal cholangiocarcinoma. H&E examination confirmed that 4 cases were well-differentiated adenocarcinoma, 15 cases were moderately differentiated adenocarcinoma, 9 cases were poorly differentiated adenocarcinoma, and 3 cases were undifferentiated carcinoma. Of the 31 cancers, 13 were categorized as low-grade TB cases and 18 as high-grade TB. The 13 low-grade TB cases included 4 well-differentiated adenocarcinomas, 8 moderately differentiated adenocarcinomas, and one poorly differentiated adenocarcinoma. The 18 high-grade TB cases included 7 moderately differentiated adenocarcinomas, 8 poorly differentiated adenocarcinomas, and 3 undifferentiated carcinomas.

## 3D analysis of adenocarcinomas

All 31 cases were successfully cleared and immunolabeled to observe 3D morphology. All cases were examined by light sheet microscopy (4× objective) to determine the region of tumor buds in 3D. Next, details of structures were examined in all cases using confocal laser scanning microscopy (10×, 20× objectives). 3-D imaging revealed that the main tumor of adenocarcinomas, but not undifferentiated carcinomas, were composed of complex interconnecting tubules and cords. ‘Tubules’ were defined as lumen-forming projections of carcinoma. ‘Cords’ were defined as thread/rope-like solid (non–lumen-forming) projections of the carcinoma. ‘Protrusions’ were defined as an extension of the carcinoma composed of greater than four cells from the main mass. Each tubule and cord structure was composed of a disorganized irregular CK19–positive epithelial cells. These neoplastic structures could easily be distinguished from normal bile duct by their irregular and complex 3D architecture. Protrusions formed tubules and/or cords (Figure 1A–D).

DAPI and CK19 labeling was performed to determine which would be better for counting cell numbers in tumor buds. We counted cell numbers randomly at the tips of 15 protrusions qualified for tumor buds (five protrusions per a case, three high-grade TB adenocarcinomas), and compared DAPI and CK19 cell counts at the same locations. We chose to analyze high-grade TB adenocarcinomas, because of the large number of protrusions available for analysis in each case. Counting cells using DAPI nuclear labeling gave a mean of 2.64 cells (range 1–4 cells), and cells using CK19 labeling (the non-labeling centers of the cells served to define nuclei) gave a mean of 2.78 cells (range 2–4 cells, supplementary material, Figure S1 A, B). Although these two methods generated comparable cell counts, we found the DAPI labeling more difficult to interpret, because the nuclei of non-neoplastic cells, including inflammatory cells, labeled with DAPI and the signals from the non-neoplastic cells and the neoplastic cells often overlapped (supplementary material, Figure S1C). In subsequent experiments, we therefore used CK19 labeling only to count cells.

## 3D analysis of adenocarcinomas with low-grade TB

Cases with low-grade TB were characterized in 2D H&E sections as gland-forming adenocarcinomas without or with at most minimal budding (Figure 2A). In the 3D

images, the main tumor of these carcinomas was composed predominantly of complex interconnecting tubules, and multiple lumens were observed in the main tumor. At the periphery of the tumors, there were a few short protrusions, and these were primarily tubules, the tips of which often transitioned into short cords. Detached clusters of neoplastic cells and single cells were not observed (Figure 2B and supplementary material, Movie S1).

### 3D analysis of adenocarcinomas with high-grade TB

High-grade TB cases included 15 adenocarcinomas and 3 undifferentiated carcinomas, and these two groups had different morphologies. In 2D H&E sections, the 15 adenocarcinomas were characterized by a mixture of gland-forming areas and areas of cord-like or single-cell growths. Multiple tumor buds were observed at the periphery of these carcinomas. These tumor buds appeared to be detached from the main tumor and embedded in and completely surrounded by stroma (Figure 2C). 3D analysis of these 15 adenocarcinomas with high-grade TB revealed that tumor buds corresponded to the tips of contiguous attenuated protrusion which, on cross-section, contained four cells or fewer. The main tumors were composed primarily of complex interconnecting cords, and tubules were rare. As the protrusions branched they became attenuated, and in cross-section these gave the impression of discontinuous islands of cells (tumor buds) (Figure 2D and supplementary material, Movie S2, supplementary material, Figures S1–S3). Compared with the adenocarcinomas with low-grade TB, the protrusions of adenocarcinomas with high-grade TB were more numerous and longer, with more complex branching.

### 3D analysis of undifferentiated carcinomas with high-grade TB

In 2D H&E sections, undifferentiated carcinomas showed single cells and clusters of neoplastic cells embedded in the stroma without any gland formation (Figure 3A). 3D analysis of the cleared tissues revealed sheets of neoplastic cells without tubular formation. Toward the periphery of the tumor, neoplastic cells were discohesive, with sheets of neoplastic cells forming small clusters of cells and eventually separate single cells (Figure 3B). Surface rendering highlighted sheets of small clusters and separate single neoplastic cells (Figure 3C, D and supplementary material, Movie S3). In 3D the tumor buds of undifferentiated carcinoma corresponded to detached isolated neoplastic cells composed of four cells or fewer, and there was no connection of these cells with the main tumor.

### Serial images of adenocarcinoma with high-grade TB

Serial 2D images (every 9 μm) of the thick slabs of tissue using confocal laser scanning microscopy showed how contiguous structures in 3D could appear as discontinuous islands in 2D. In 2D the thin sections of the branching contiguous structures appeared as multiple detached small clusters and single cells (Figure 4A–F, supplementary material, Figures S2, S3).

### E-cadherin expression in low- and high-grade TB cases

In low-grade TB cases, double immunofluorescence labeling with E-cadherin (red) and CK19 (green) showed intact E-cadherin expression in the neoplastic cells in the center of the tumor. By contrast, E-cadherin expression was attenuated at the periphery of the neoplastic

protrusions (Figure 5A–C). In the high-grade TB cases, co-expression of E-cadherin and CK19 was again seen in the neoplastic cells in the center of the tumor. E-cadherin expression was also lost in the periphery of the neoplastic protrusions. The extent of peripheral loss was greater in high-grade TB cases than in low-grade TB cases (Figure 5D–F).

Surface rendering images highlighted strong E-cadherin expression in the center of the tumors. In contrast, expression of E-cadherin disappeared at the tips of the tumor protrusions. Areas of E-cadherin loss were again seen to be more extensive in high-grade TB cases than in low-grade TB cases (Figure 5G–J, and supplementary material, Movies S4, S5). These observations were confirmed by quantitative image analysis (see below).

## Filament tracer analysis and volume calculating analysis using surface rendering

Although the antibody penetration into the cleared tissue was adequate for 3D observations in all cases, the quantitative analyses performed using IMARIS software required strong and even luminosity, which was best achieved when there was deep and uniform penetration of antibodies into the cleared tissue. The depth of antibody penetration was variable from case to case, and we restricted our quantitative analyses to the 12 cases with clear uniform antibody penetration. This resulted in sharp border lines between stained and unstained structures recognizable by the software. We performed filament tracer analysis on 12 cases, including 6 adenocarcinomas with low-grade TB (3 well-differentiated adenocarcinomas and 3 moderately differentiated adenocarcinomas) and 6 adenocarcinomas with high-grade TB (2 moderately differentiated adenocarcinomas and 4 poorly differentiated adenocarcinomas) to compare between two groups. Eleven regions in total (one or two regions per case) were analyzed in each group. Regions were selected based on the area of TB in matched H&E sections. First, the branch points in protrusions were counted. High-grade TB had more branch points than did low-grade TB (median, 26 versus 20, $p = 0.021$). Next, the average length of a protrusion was measured. When a protrusion has branches, the length of all branches was summed. When calculated in this manner, high-grade TB had longer protrusions than did low-grade TB (median, 53.3 versus 32.1 μm, $p < 0.001$) (Figure 6A, B).

We also performed volume calculating analysis on 12 cases described above. Ten regions in total (one or two regions per case) in each group were analyzed using volume calculating analysis of IMARIS software. The volume ratio of E-cadherin/CK19 expression represents the volume ratio of neoplastic cells expressing both E-cadherin/CK19. The volume ratio of E-cadherin/CK19 expression was lower in high-grade TB than in low-grade TB (median, 0.65 versus 0.81, $p = 0.0052$) (Figure 6C). The finding that high-grade TB cases lose E-cadherin expression more is consistent with more EMT in these cancers.

## E-cadherin expression in undifferentiated carcinoma

The expression of E-cadherin in the undifferentiated carcinoma was almost completely lost in the neoplastic cells and observed only in the epithelium of non-neoplastic bile ducts overtaken by the cancer (supplementary material, Figure S4A–D).

## Discussion

In this study of cleared cholangiocarcinoma, we comprehensively integrated the 3D architecture of TB with E-cadherin expression. We found that the neoplastic cells in tumor buds were not individual islands of neoplastic cells, but rather tips of contiguous attenuated protrusions extending form the main tumor. In 2D cross-sections, these connected branching protrusions appeared to be small clusters or single cells completely surrounded by stroma. Bronsert *et al* came to similar conclusions when they described the 3D architecture of the tumor buds of human adenocarcinomas using reconstruction of serial immunohistochemically labeled 2-D slides [27]. Their study included, in total, 15 adenocarcinoma cases, 3 cases each from five organs (pancreas, colorectum, metastatic colorectal adenocarcinoma to liver, lung, and breast). Here we studied the 3D architecture of cholangiocarcinoma and analyzed differences between high-grade and low-grade-TB cases. In our study, tissue clearing with immunolabeling made it possible to examine intact tissue using fluorescent microscopy.

Using clearing, we were able to delineate 3D structural differences between high-grade TB and low-grade TB. We found that both high-grade and low-grade TB adenocarcinomas formed tubules and cords. The low-grade TB cases predominantly formed tubules; when they formed cords, the cords were at the leading edges of the tumors. By contrast, the high-grade TB cases predominantly formed cords, which were observed both at the center of the tumors as well as at the periphery. In addition, differences were observed in the complexity and overall length of protrusions. There was more branching, and the protrusions were longer, in high-grade TB cases than in low-grade TB cases. This complexity explains the appearance of greater TB in 2D sections.

In 2D analysis, undifferentiated carcinoma lacked gland formation, and all three cases included in our study were classified as high-grade TB cases. We observed that the 3D architecture of undifferentiated carcinoma is characterized by detached small clusters and single cells, a pattern totally different from the gland-forming adenocarcinoma cases. This finding differs somewhat from Bronsert's 3D study, as they were unable to find single cell migration in the 15 tumors they examined; however, this could be due to the relatively small number of samples they studied as well the absence of undifferentiated carcinomas in their series of cases [27]. Thus, single cells can occur, but they must be relatively rare events.

Two types of cancer cell migration have been described at the leading edges of carcinomas; one is collective cell migration and the other is individual cell migration [32]. In the case of collective invasion, the leading cells have partial mesenchymal characteristics and invade into the stroma accompanied by peri-cellular proteolysis [33,34]. Proteolysis was thought to make single cells detach from the main tumor and infiltrate into the stroma. However, recent studies have revealed that single cell invasion is a relatively rare event [35]. Our findings support the hypothesis that most cancer cells infiltrate with connected branching protrusions that extend into connective tissue, mimicking collective invasion. Only rare types of cancer, such as undifferentiated carcinoma, infiltrate as detached singe cells.

EMT is a process in which epithelial cells lose their cell–cell adhesion and gain migratory properties typically seen in mesenchymal cells [36]. EMT has been hypothesized to play a role in cancer invasion and metastasis. A hallmark of EMT is downregulation of the expression of the cell adhesion molecule E-cadherin, which is a transmembrane protein that is vital for adherent junctions, accompanied by the upregulation of mesenchymal molecules such as ZEB1, ZEB2, TWIST, or vimentin [37]. It has been hypothesized that TB is related to EMT because the membrane localization and expression of E-cadherin are relatively low in the cells of tumor buds, and the cells appear in 2D to be detached from the main tumor [12,15,27,38]. Our 3D imaging analysis revealed that the expression of E-cadherin is attenuated only focally, at the tips of protrusions. We also quantified E-cadherin and found that the loss of E-cadherin is greater in high-grade TB cases than it is in low-grade TB cases. The poor prognosis of high-grade TB cases may be related to more neoplastic cells being in the state of focal, or possibly transient, EMT [39]. These findings with quantitative volume measurement highlight the importance of analyzing diseases in 3D.

There were several limitations in the present study. First, because of the complexities of large 3D structures and focally incomplete antibody penetration deep in tissues, we were not able to quantify our qualitative observations for all cases. In the future we hope to improve the antibody penetration techniques, standardize the 3D images, and obtain quantitative data to more precisely measure the differences observed. Second, although the decreased expression of E-cadherin is critical, additional markers of EMT, such as ZEB1, TWIST, or vimentin, will help solidify EMT status in these cancers [40].

In conclusion, this study provides comprehensive analysis of 3D architecture and E-cadherin distribution in cholangiocarcinoma. We find that TB is a reflection of attenuated, but contiguous, protrusions extending from the main tumor. High-grade TB cases show more complex branching and longer length of protrusions, as well as more extensive E-cadherin loss at the leading edge of protrusions. These results provide a deeper understanding of the structural and molecular processes underlining tumor invasion, enabling future studies to further dissect the mechanism of metastasis in cholangiocarcinoma.

## Supplementary Material

Refer to Web version on PubMed Central for supplementary material.

## Acknowledgements

The study was supported by Mary M. Graf Memorial Endowment for gallbladder cancer at Johns Hopkins University. The authors thank Dr. Wojciech B. Zbijewski for advice regarding image analysis, Dr. Daniel M. Raben for advice regarding chemical solvent of tissue clearing, and Ms. Yuan Cai for technical support.

## References

1. Ueno H, Murphy J, Jass JR, et al. Tumour “budding” as an index to estimate the potential of aggressiveness in rectal cancer. Histopathology 2002; 40: 127–132. [PubMed: 11952856]
2. Koelzer V, Zlobec I, Lugli A. Tumor budding in colorectal cancer— ready for diagnostic practice? Hum Pathol 2016; 47: 4–19. [PubMed: 26476568]

3. Tanaka K, Shimura T, Kitajima T, et al. Tropomyosin-related receptor kinase B at the invasive front and tumour cell dedifferentiation in gastric cancer. Br J Cancer 2014; 110: 2923–2934. [PubMed: 24853179]
4. Gulluoglu M, Yegen G, Ozluk Y, et al. Tumor budding is independently predictive for lymph node involvement in early gastric cancer. Int J Surg Pathol 2015; 23: 349–358. [PubMed: 25911564]
5. Che K, Zhao Y, Qu X, et al. Prognostic significance of tumor budding and single cell invasion in gastric adenocarcinoma. Onco Targets Ther 2017; 10: 1039–1047. [PubMed: 28255247]
6. Olsen S, Jin L, Fields RC, et al. Tumor budding in intestinal-type gastric adenocarcinoma is associated with nodal metastasis and recurrence. Hum Pathol 2017; 68: 26–33. [PubMed: 28428104]
7. Kemi N, Eskuri M, Ikäläinen J, et al. Tumor budding and prognosis in gastric adenocarcinoma. Am J Surg Pathol 2019; 43: 229–234. [PubMed: 30334831]
8. Koike M, Kodera Y, Itoh Y, et al. Multivariate analysis of the pathologic features of esophageal squamous cell cancer: tumor budding is a significant independent prognostic factor. Ann Surg Oncol 2008; 15: 1977–1982. [PubMed: 18408975]
9. Miyata H, Yoshioka A, Yamasaki M, et al. Tumor budding in tumor invasive front predicts prognosis and survival of patients with esophageal squamous cell carcinomas receiving neoadjuvant chemotherapy. Cancer 2009; 115: 3324–3334. [PubMed: 19452547]
10. Nakanishi Y, Ohara M, Doumen H, et al. Correlation between tumor budding and post-resection prognosis in patients with invasive squamous cell carcinoma of the thoracic esophagus. World J Surg 2011; 35: 349–356. [PubMed: 21132295]
11. Karamitopoulou E, Zlobec I, Born D, et al. Tumour budding is a strong and independent prognostic factor in pancreatic cancer. Eur J Cancer 2013; 49: 1032–1039. [PubMed: 23177090]
12. Kohler I, Bronsert P, Timme S, et al. Detailed analysis of epithelial-mesenchymal transition and tumor budding identifies predictors of long-term survival in pancreatic ductal adenocarcinoma. J Gastroenterol Hepatol 2015; 30: 78–84. [PubMed: 25827809]
13. O'Connor K, Li-Chang HH, Kalloger SE, et al. Tumor budding is an independent adverse prognostic factor in pancreatic ductal adenocarcinoma. Am J Surg Pathol 2015; 39: 472–478. [PubMed: 25634751]
14. Ohike N, Coban I, Kim GE, et al. Tumor budding as a strong prognostic indicator in invasive ampullary adenocarcinomas. Am J Surg Pathol 2010; 34: 1417–1424. [PubMed: 20871215]
15. Almangush A, Salo T, Hagstrom J, et al. Tumour budding in head and neck squamous cell carcinoma - a systematic review. Histopathology 2014; 65: 587–594. [PubMed: 24897954]
16. Boxberg M, Kuhn P, Reiser M, et al. Tumorbudding and cell nest size are highly prognostic in laryngeal and hypopharyngeal squamous cell carcinoma further evidence for a unified histopathologic grading system for squamous cell carcinomas of the upper aerodigestive tract. Am J Surg Pathol 2019; 43: 303–313. [PubMed: 30475254]
17. Yamakawa N, Kirita T, Umeda M, et al. Tumor budding and adjacent tissue at the invasive front correlate with delayed neck metastasis in clinical early-stage tongue squamous cell carcinoma. J Surg Oncol 2019; 119: 370–378. [PubMed: 30548537]
18. Zhang S, Wang X, Gupta A, et al. Expression of IL-17 with tumor budding as a prognostic marker in oral squamous cell carcinoma. Am J Transl Res 2019; 11: 1876–1883. [PubMed: 30972211]
19. Chatterjee D, Bansal V, Malik V, et al. Tumor budding and worse pattern of invasion can predict nodal metastasis in oral cancers and associated with poor survival in early-stage tumors. Ear Nose Throat J 2019; 98: 112–119.
20. Liang F, Cao W, Wang Y, et al. The prognostic value of tumor budding in invasive breast cancer. Pathol Res Pract 2013; 209: 269–275. [PubMed: 23561623]
21. Lorenzo Soriano L, Ordaz Jurado G, Pontones Moreno JL, et al. Tumor budding: prognostic value in muscle-invasive bladder cancer. Urology 2019; 130: 93–98. [PubMed: 30986485]
22. Ogino M, Nakanishi Y, Mitsuhashi T, et al. Impact of tumor budding grade in 310 patients who underwent surgical resection for extrahepatic cholangiocarcinoma. Histopathology 2019; 74: 861–872. [PubMed: 30667537]
23. Okubo S, Mitsunaga S, Kato Y, et al. The prognostic impact of differentiation at the invasive front of biliary tract cancer. J Surg Oncol 2018; 117: 1278–1287. [PubMed: 29572828]

24. Tanaka M, Yamauchi N, Ushiku T, et al. Tumorbudding in intrahepatic cholangiocarcinoma a predictor of postsurgery outcomes. Am J Surg Path 2019; 43: 1180–1190. [PubMed: 31335353]
25. De Smedt L, Palmans S, Andel D, et al. Expression profiling of budding cells in colorectal cancer reveals an EMT-like phenotype and molecular subtype switching. Br J Cancer 2017; 116: 58–65. [PubMed: 27884016]
26. Zlobec I, Lugli A. Tumour budding in colorectal cancer: molecularrationale for clinical translation. Nat Rev Cancer 2018; 18: 203–204. [PubMed: 29376521]
27. Bronsert P, Enderle-Ammour K, Bader M, et al. Cancer cell invasion and EMT marker expression: a three-dimensional study of the human cancer-host interface. J Pathol 2014; 234: 410–422. [PubMed: 25081610]
28. Tanaka N, Kanatani S, Tomer R, et al. Whole-tissue biopsy phenotyping of three-dimensional tumours reveals patterns of cancer heterogeneity. Nat Biomed Eng 2017; 1: 796–806. [PubMed: 31015588]
29. Noë M, Rezaee N, Asrani K, et al. . Immunolabeling of cleared human pancreata provides insights into three-dimensional pancreatic anatomy and pathology. Am J Pathol 2018; 188: 1530–1535. [PubMed: 29684363]
30. Hong SM, Noë M, Hruban CA, et al. A “clearer” view of pancreatic pathology: a review of tissue clearing and advanced microscopy techniques. Adv Anat Pathol 2019; 26: 31–39. [PubMed: 30256228]
31. Jessup JM, Goldberg RM, Asare EA, et al. Colon and Rectum. In AJCC Cancer Staging Manual (8th edn), Amin M (ed). Springer: Chicago, 2017; 251–274.
32. Friedl P, Alexander S. Cancer invasion and the microenvironment: plasticity and reciprocity. Cell 2011; 147: 992–1009. [PubMed: 22118458]
33. Gaggioli C, Hooper S, Hidalgo-Carcedo C, et al. Fibroblast-led collective invasion of carcinoma cells with differing roles for RhoGTPases in leading and following cells. Nat Cell Biol 2007; 9: 1392–1400. [PubMed: 18037882]
34. Khalil AA, Friedl P. Determinants of leader cells in collective cellmigration. Integr Biol 2010; 2: 568–574.
35. Cheung KJ, Gabrielson E, Werb Z, et al. Collective invasion in breast cancer requires a conserved basal epithelial program. Cell 2013; 155: 1639–1651. [PubMed: 24332913]
36. Pearson GW. Control of invasion by epithelial-to-mesenchymal transition programs during metastasis. J Clin Med 2019; 8: 646. [PubMed: 31083398]
37. Williams ED, Gao D, Redfern A, et al. Controversies around epithelial–mesenchymal plasticity in cancer metastasis. Nat Rev Cancer 2019; 19: 716–732. [PubMed: 31666716]
38. Attramadal CG, Kumar S, Boysen ME, et al. Tumor budding, EMT and cancer stem cells in T1–2/N0 oral squamous cell carcinomas. Anticancer Res 2015; 35: 6111–6120. [PubMed: 26504037]
39. Hong SM, Jung D, Kiemen A, et al. Three-dimensional visualization of cleared human pancreas cancer reveals that sustained epithelial-to-mesenchymal transition is not required for venous invasion. Mod Pathol 2019; 33: 639–647. [PubMed: 31700162]
40. Onder TT, Gupta PB, Mani SA, et al. . Loss of E-cadherin promotes metastasis via multiple downstream transcriptional pathways. Cancer Res 2008; 68: 3645–3654. [PubMed: 18483246]

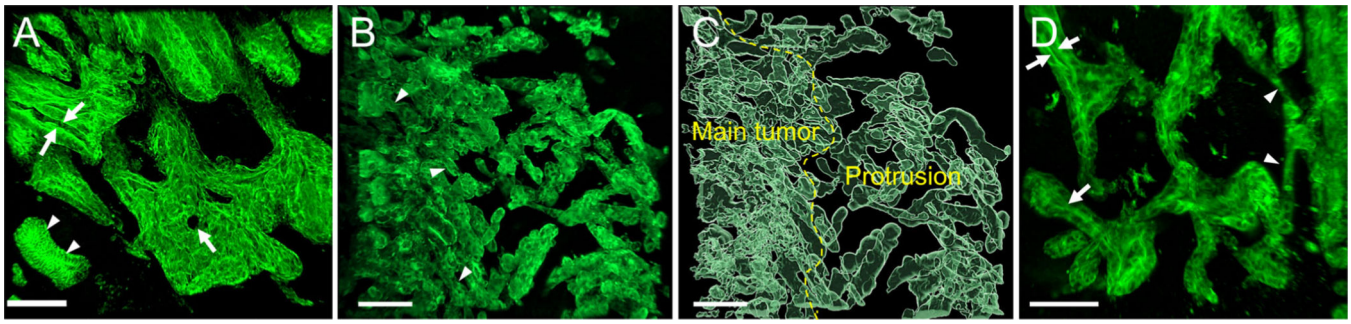


**Figure 1.**

3D image of adenocarcinomas. (A) The main tumor was composed predominantly of tubules lined with irregular disorganized epithelium. The lumens in the tubules (arrows) were identified. Note the adjacent normal bile duct (arrowheads) (low-grade TB, confocal laser scanning microscope). (B) The main tumor was composed predominantly of complex interconnecting cords (arrowheads) (high-grade TB, confocal laser scanning microscope). (C) The main tumor and protrusions (surface rendering image). (D) Higher magnification of the periphery of tumor showing protrusions. Protrusion may form tubule (arrows) or cords (arrowheads) (surface rendering image, scale bar, 100 μm).

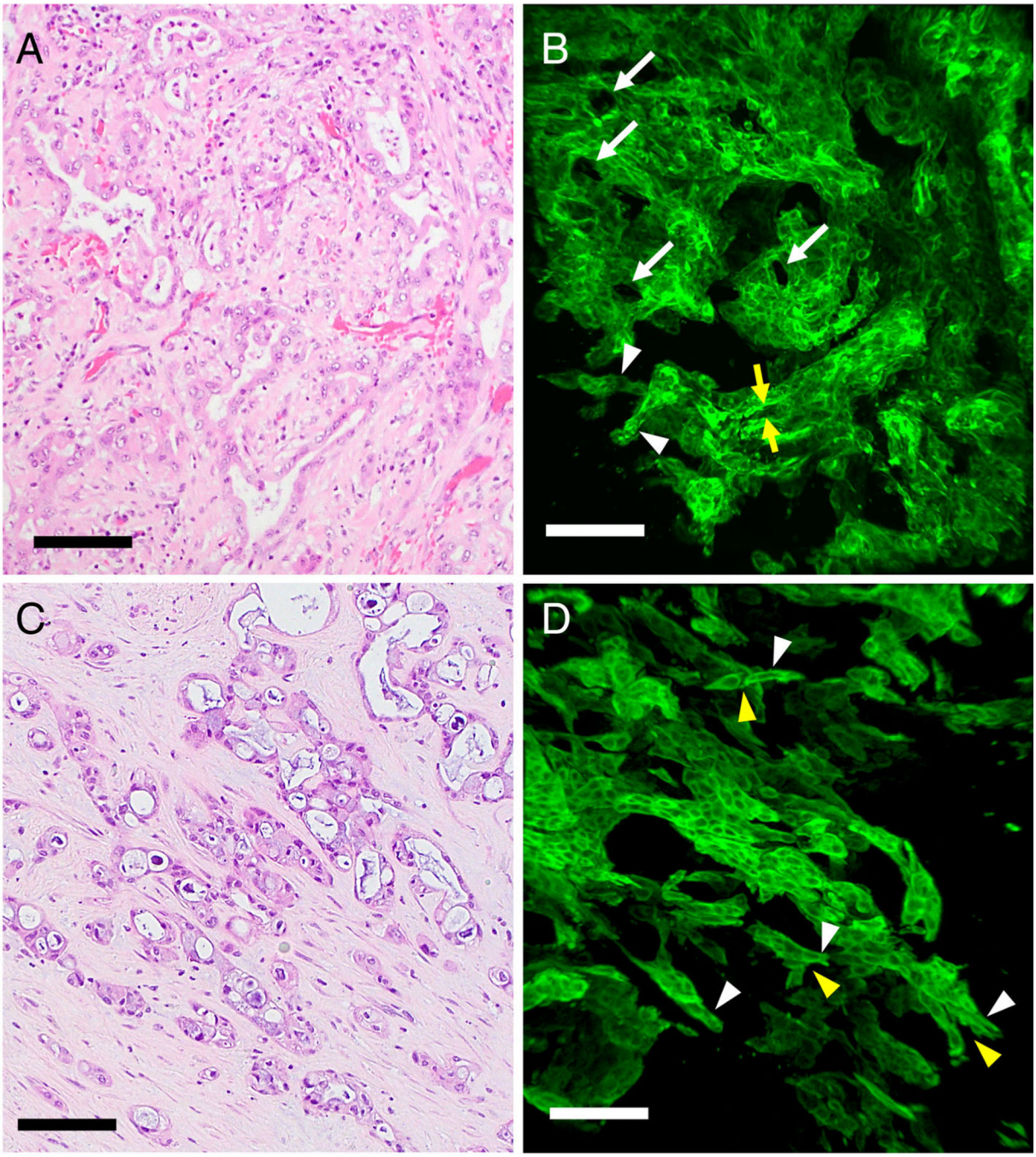


**Figure 2.**

Low-grade TB and high-grade TB of adenocarcinoma cases. (A) H&E staining of low-grade TB case. The tumor was composed predominantly of anastomosing neoplastic glands. TB was not observed in this case. (B) 3D image of a low-grade TB case (confocal laser scanning microscope). The tumor was composed of mainly interconnecting tubules, and cross-sections of multiple lumens were observed in the main tumor (arrows). The tubule (yellow arrows) was transitioned into short cords (arrowheads), and a few cords were noted at the periphery. (C) H&E staining of a high-grade TB adenocarcinoma case. Carcinoma

showed the area of glandular formation as well as sheet of neoplastic cells and single cells. (D) 3D image of a high-grade TB adenocarcinoma case. The tubular formation was not obvious in the tumor. There were multiple protrusions with branching. The branching points were observed (yellow arrow heads). The protrusions were predominantly cord-like structure (arrowheads) (confocal laser scanning microscope) (scale bar, 100 μm).

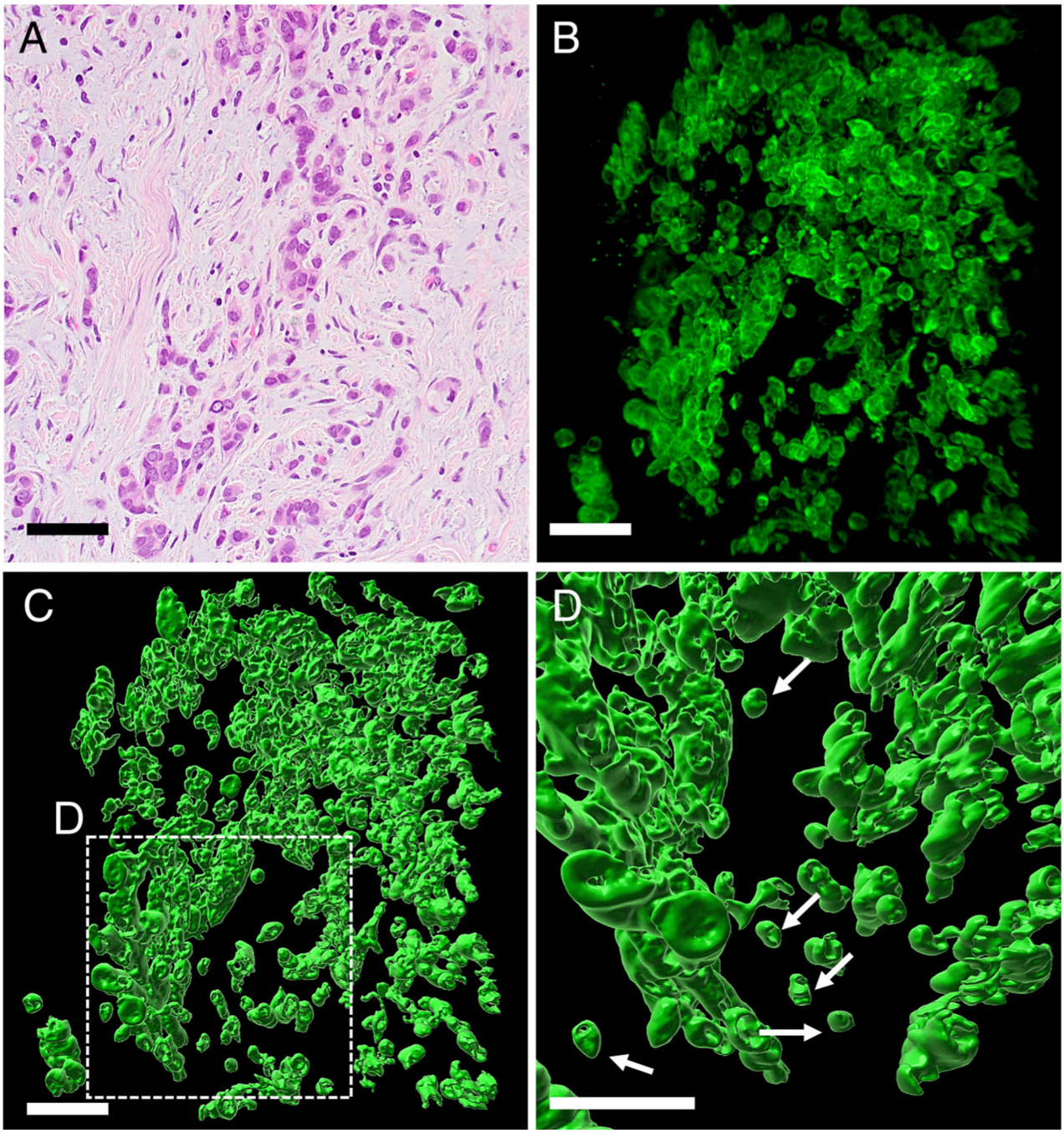


**Figure 3.**

High-grade TB of undifferentiated carcinoma cases. (A) H&E staining showed small clusters tumor cells and single cells invading the stroma without glandular formation. (B) 3D image of undifferentiated carcinoma (confocal laser scanning microscope). The tumor was composed of sheet of neoplastic cells. Toward the periphery, the tumor became discohesive, with neoplastic cells forming small clusters of cells and eventually single cells. (C) Detached clusters of cells and single cells were noted (surface-rendering image). (D) High magnification of undifferentiated carcinoma at the periphery of tumor in the region

shown in C (surface-rendering image). Detached single cells (arrows) were noted (scale bar, 100 μm).

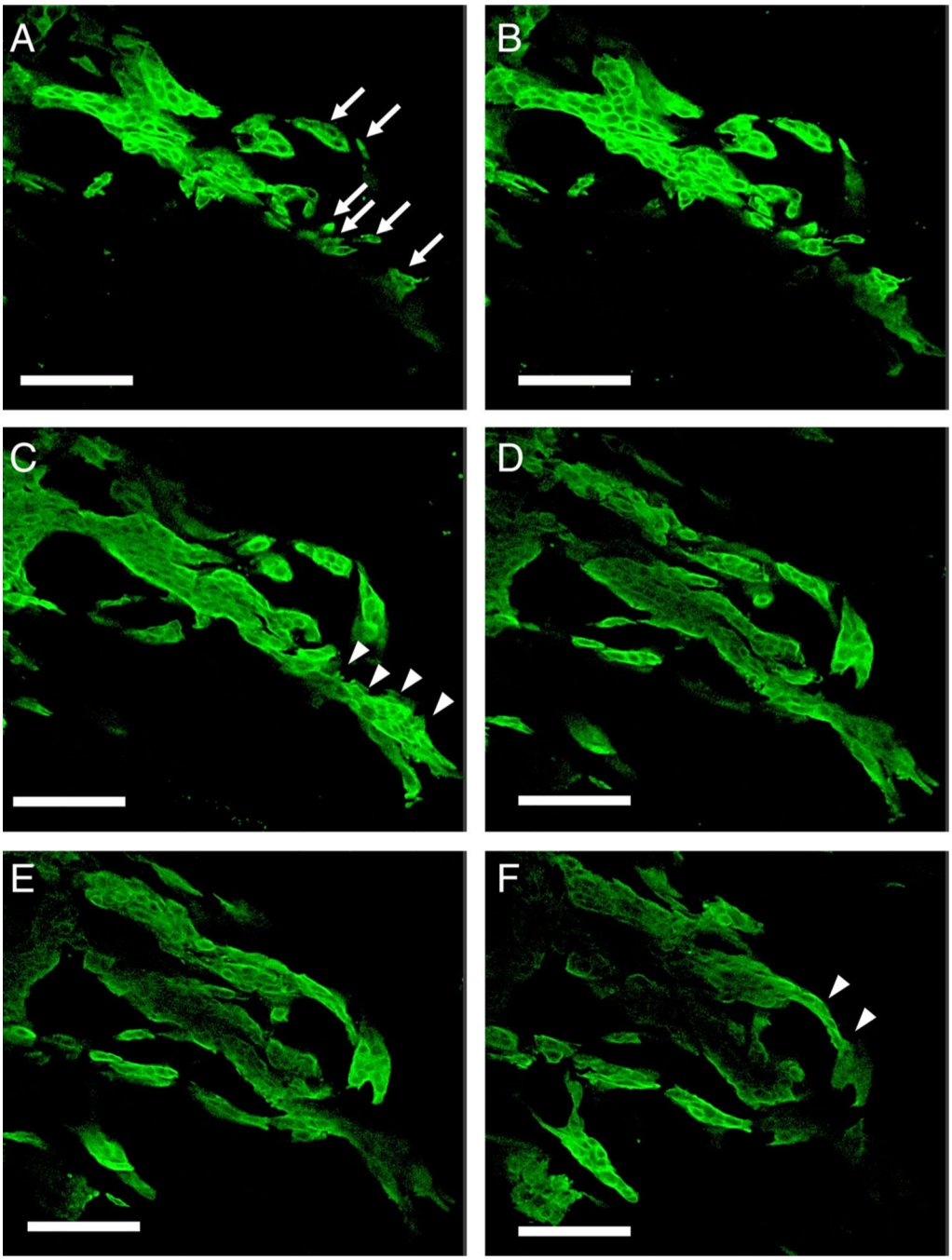


**Figure 4.**

Serial sections of a high-grade TB adenocarcinoma case (images every 9 μm) (confocal laser scanning microscope). (A) Tumor buds were found as detached small clusters of neoplastic cells and single cells (arrows). (B–F) Serial sections showing that isolated clusters and a single cell were connected to the main tumor (arrowhead) (scale bar, 100 μm).

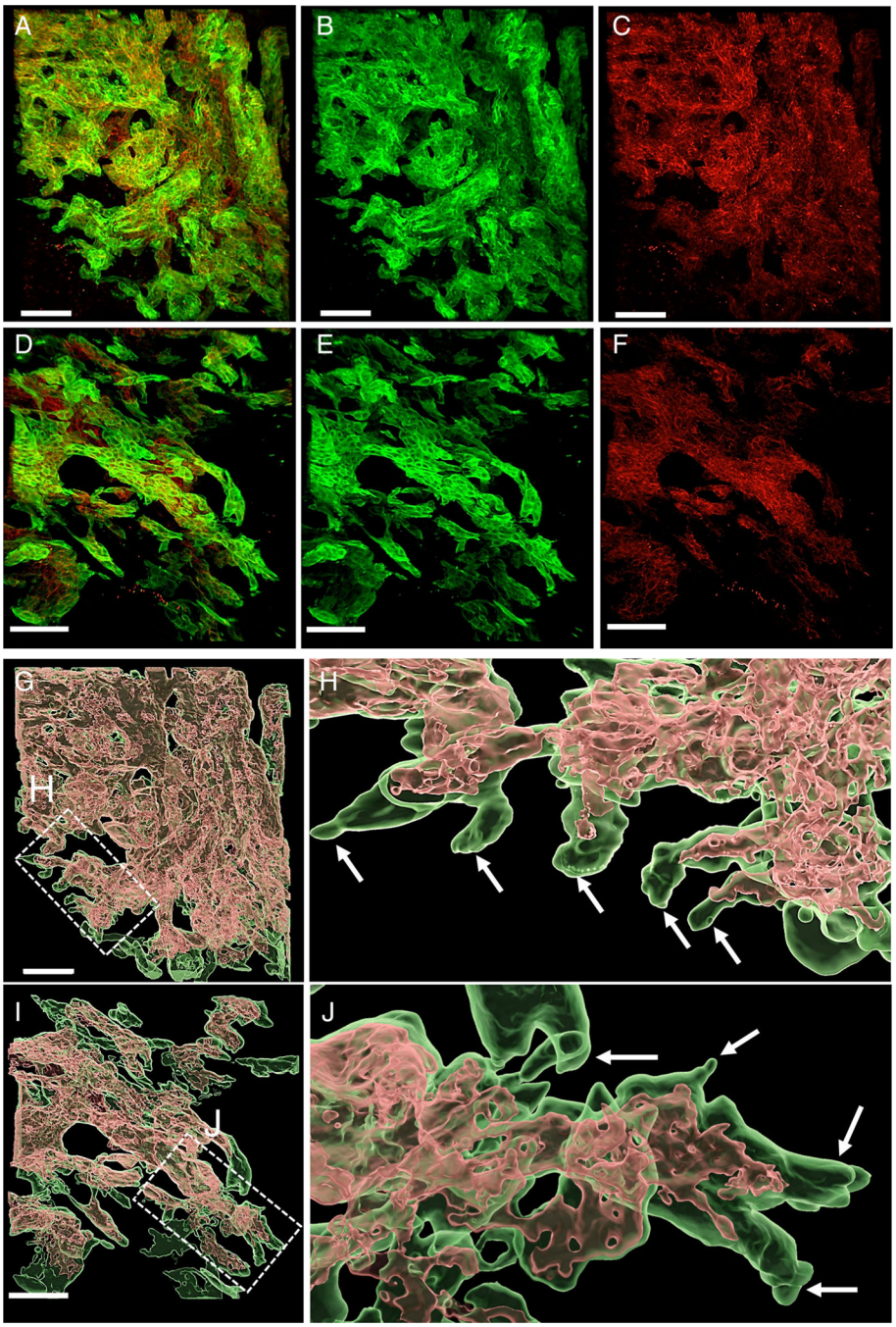


**Figure 5.**

CK19 and E-cadherin expression in a low-grade TB case (A–C) and a high-grade TB case (D–F) (confocal laser scanning microscopy). (A) CK19 and E-cadherin merged image in a low-grade TB case. (B) CK19 (green) image. (C) E-cadherin (red) image. (D) CK19 and E-cadherin merged image in a high-grade TB case. (E) CK19 (green) image. (F) E-cadherin (red) image. E-cadherin loss was more extensive in the high-grade TB case than the low-grade TB case at the periphery of the tumor. Surface-rendering image of CK19 and E-cadherin expression (G–J). (G) Low-grade TB case. Co-expression of CK19 (green) and

E-cadherin (red) was present at the center of the tumor. (H) Higher magnification of the low-grade TB case at the periphery. Loss of E-cadherin expression was noted at the tips of protrusions. (I) High-grade TB case. Co-expression of CK19 (green) and E-cadherin (red) was also present at the center of the tumor. (J) E-cadherin loss at the protrusions was more extensive in the high-grade TB case than in the low-grade TB case (scale bar, 100 μm).

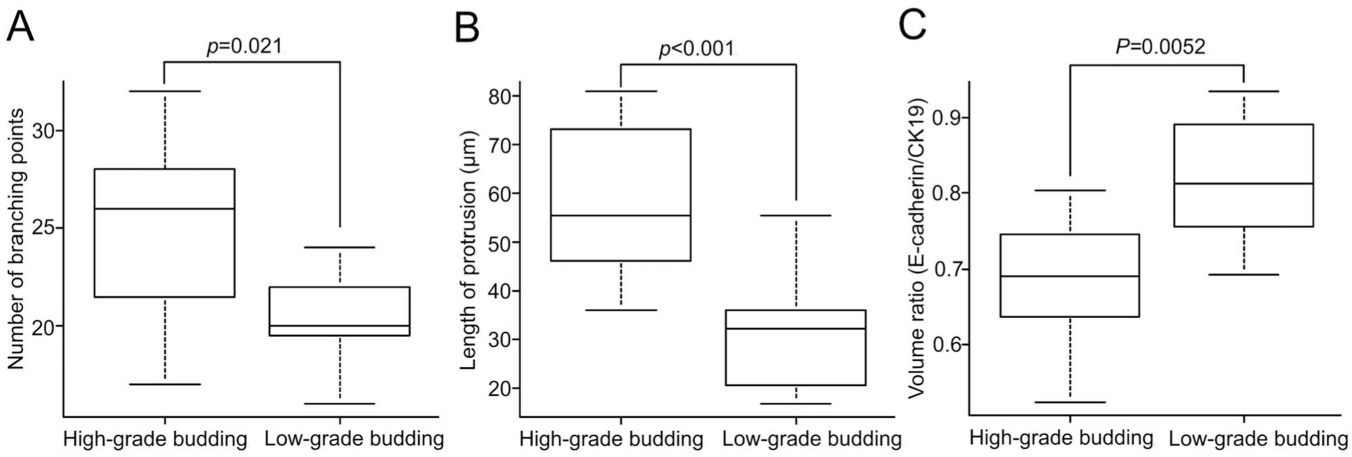


**Figure 6.**

Filament tracer analysis and volume calculating analysis for protrusion. (A) The number of branching points in protrusions was more in high-grade TB than in low-grade TB case ($p$ = 0.021). (B) The length of protrusion was longer in high-grade TB than low-grade TB case ($p$ < 0.001). (C) Volume ratio of E-cadherin/CK19 expression of high-grade TB was lower than that of low-grade TB case ($p$ = 0.0052) (analyzed by Mann–Whitney test).